

**Cell Reports**

**Supplemental Information**

## **A Cell-Signaling Network Temporally Resolves**

### **Specific versus Promiscuous Phosphorylation**

**Evgeny Kanshin, Louis-Philippe Bergeron-Sandoval, S. Sinan Isik, Pierre Thibault, and  
Stephen W. Michnick**

## Supplemental Figures

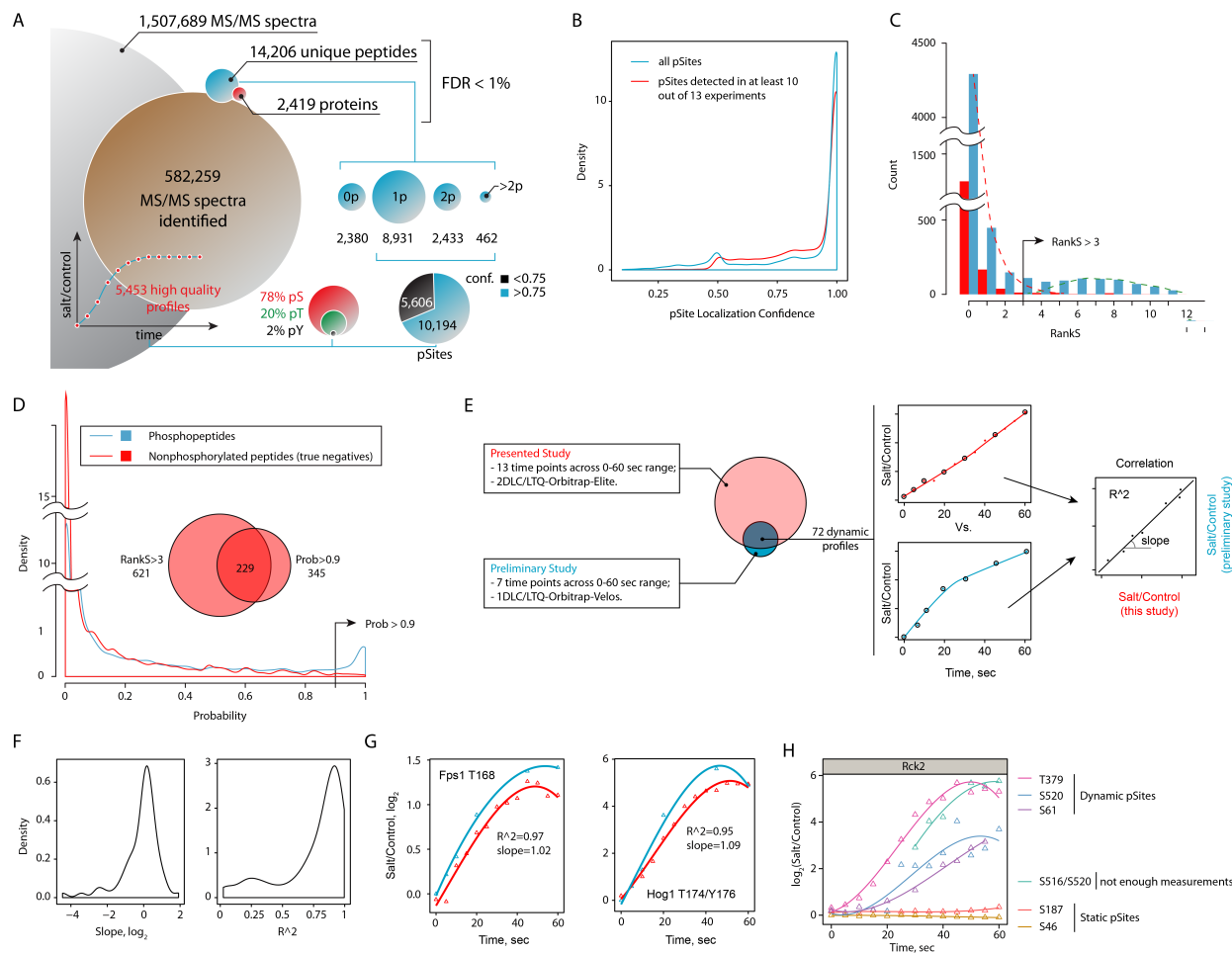


**Figure S1. Summary of phosphopeptide identification** (A) A total of 582259 MS/MS spectra were collected, which resulted in identification of 14206 unique peptides from 2419 proteins at a FDR<1%. Phosphopeptides represented 83% of all identified peptides of which 68% corresponded to phosphosite with high localization confidence ( $> 0.75$ ). A total of 3,453 dynamic profiles ( $\geq 10$  out of 13 data points/profile) were used for subsequent data analyses. (B) Density plots showing phosphosite localization confidence. Both FC-based (C) and pattern-based (D; as described in Fig. 1D-E) approaches were used to define regulated phosphosite profiles. Inset shows complementarity of these methods. (E) To address reproducibility of our approach, we examined the correlations between 72 dynamic profiles that were common for both preliminary (1DLC) and final (2DLC) data sets. Basically, FC measurements from 2 separate experiments were plotted against each other and corresponding  $R^2$  and slope values were used to access similarity between profiles. (F) Reproducibility of sub-minute phosphoproteomic kinetics in independent experiments were assessed with the distribution of  $R^2$  and "slope" parameters. We observed a correlation with a median  $R^2$  of 0.86. (G) Reproducibility between preliminary and final datasets illustrated with dynamic phosphorylation profiles of Hog1 and Fps1. (H) Profiles for all pSites on Rck2 kinase and their differentiation by our profile filtering pipeline as described in Figures 1D-E.

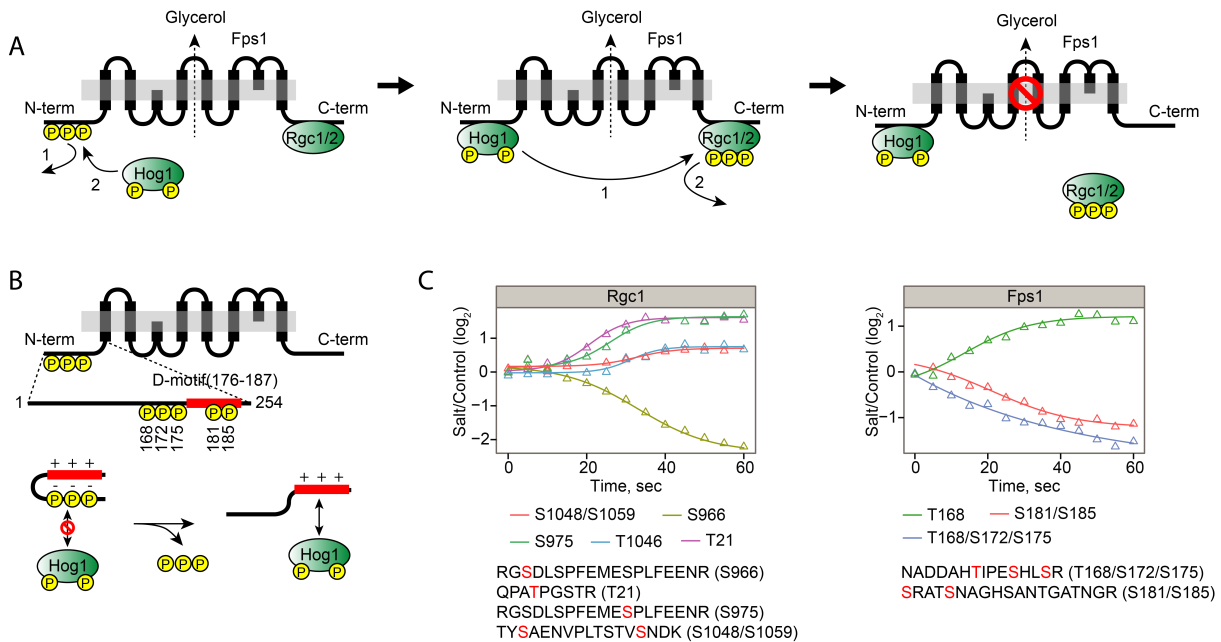


**Figure S2. Regulation of the aquaglyceroporin Fps1 in response to changes in extracellular osmolarity** (A) Model for the regulation of Fps1 by Hog1 in response to hyperosmotic shock, adapted from Lee et al. (Lee et al., 2013). Under non-stress conditions, the redundant regulators Rgc1 and Rgc2 are associated with the C-terminal domain of Fps1, and maintain Fps1 channel open. Upon osmotic shock, Hog1 is activated and recruited to the N-terminal domain of Fps1 to phosphorylate Rgc1/2, resulting in the dissociation of Rgc1/2 from the C-terminus and closure of the Fps1 channel. (B) N-terminal cytoplasmic domain of Fps1 showing the location of phosphorylation sites proximal to the MAPK docking region (D-domain). Electrostatic interactions between these phosphorylated residues and neighboring basic amino acids could prevent docking of Hog1 on D-domain. (C) Dynamic phosphorylation of Rgc1 and Fps1 residues upon osmotic shock. Fps1 phosphosites phosphodynamics show a constant increase in abundance of a monophosphorylated form that is associated with actual dephosphorylation of neighbouring sites from the triple-phosphorylated form of the same peptide. Related to Figure 2.

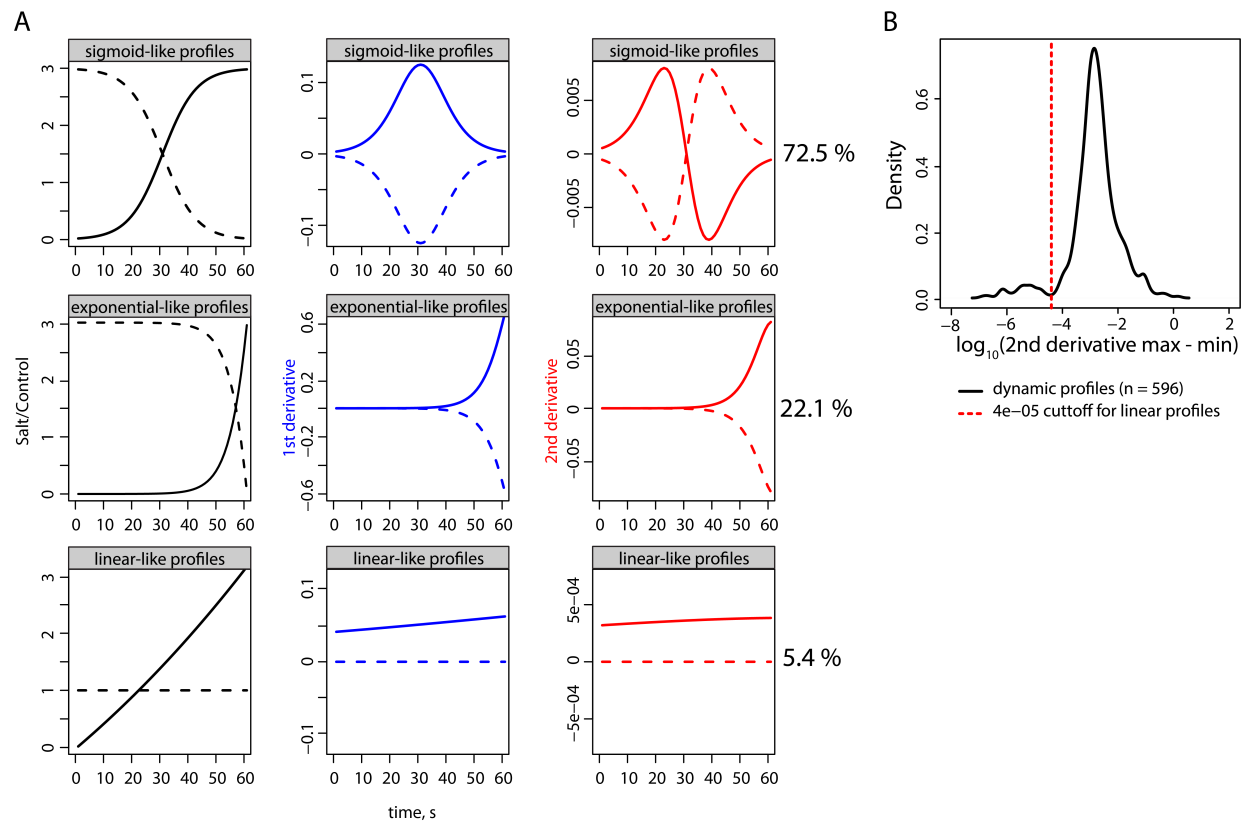


**Figure S3. Analysis of dynamic phosphorylation profiles** (A) General example of sigmoid (top), exponential (middle) and linear (bottom) shapes of fitted profiles with our birth-death model (black) along with their first derivative (blue) and second derivative (red). The shapes were sorted according to second order local max and min values and max-min difference. The occurrence of these shapes in the dynamic profiles is indicated on the left. (B) Distribution on a  $\log_{10}$  scale of the second derivative max-min difference for the dynamic profiles. We determined a cut off of 4e-05 for the max-min difference to sort linear-like profiles. Related to Figure 3.

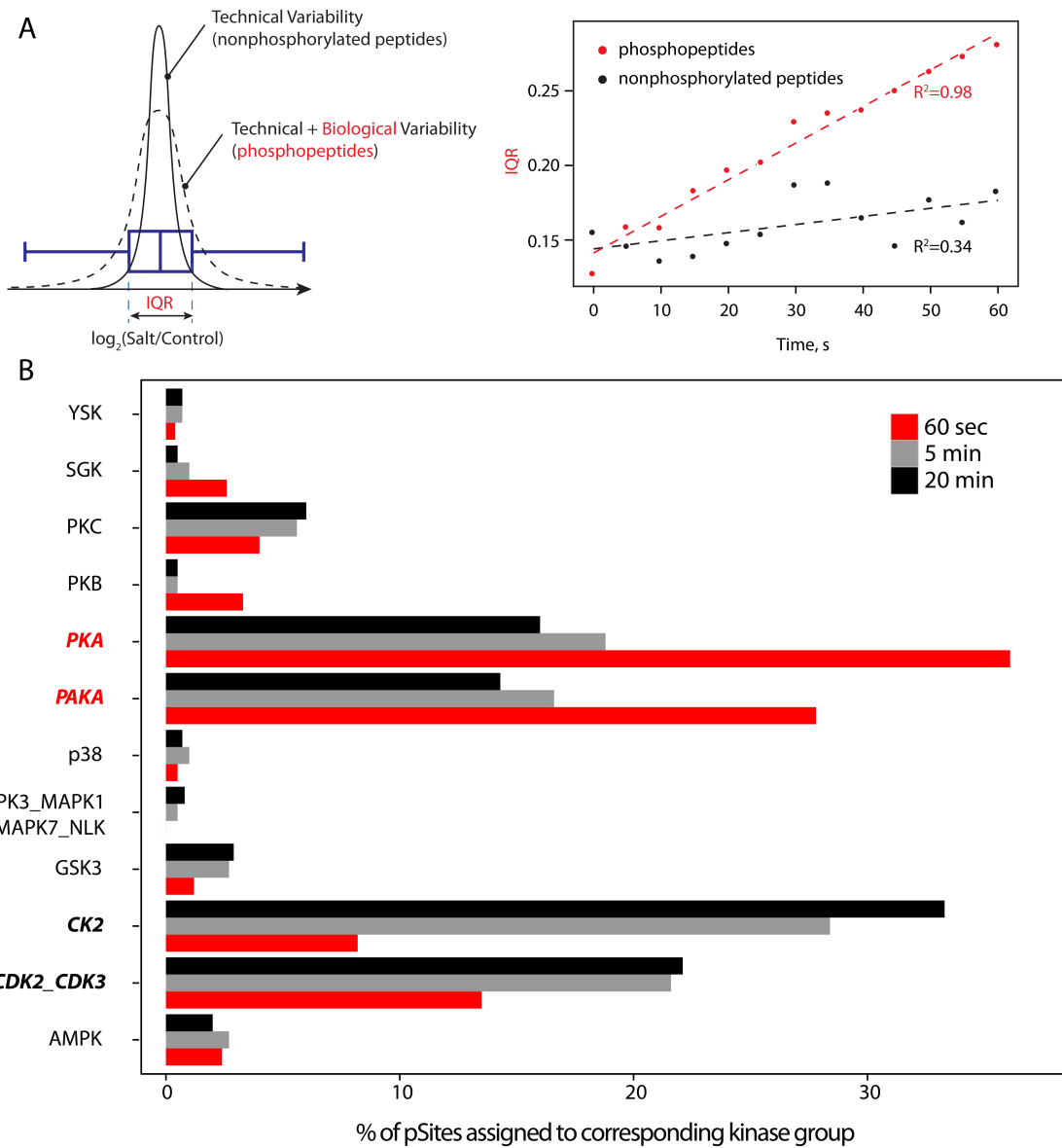


**Figure S4. Combinatorial explosion of signal complexity and kinase predictions for phosphosites** (A) Change in FC density distributions over time. We detected a constant increase in the widths of FC distribution of phosphopeptides over time, which illustrates the global effect of osmotic shock on the phosphoproteome. FC distributions of nonphosphorylated peptides remained largely unaffected and represent technical variability of our workflow (assuming protein expression is not affected within 1 minute after osmotic shock). (B). Kinase prediction for affected phosphosites in this study (60 seconds) and at 5 and 20 minutes (Soufi et al., 2009) following stimulation. Analysis was performed with PhosphoSiteAnalyzer software (Bennetzen et al., 2012), which makes predictions of kinase substrates based on the NetworKIN algorithm (Linding et al., 2008). NetworKIN applies linear motif analysis and contextual network modeling to obtain kinase-substrate associations with high accuracy and sensitivity. Related to Figure 4.



**Figure S5. Fitness of phospho-null mutants was assessed by competition-growth under high salt and non-stressed conditions.** (A) Population fractions of phospho-null mutant *versus* wild type strains were determined in competition-growth assays using specific fluorescent reporters for the respective mutant (mCherry; empty squares and magenta curve) and the wild type (EYFP; dark diamonds and grey curve) strains. A total of 18 mutant *versus* wild type binary comparisons were performed under both 1M NaCl and normal low fluorescence medium (LFM). Each graph shows the fraction of the fluorescent readout of each population and information on mutant clone identity, growth medium, kinetic category of phosphosite (Dynamic or Static) and rate of evolution of the mutated phosphosite. (B) Impact of phosphosite mutation on strain fitness is shown by a change in population fraction mean amplitude. Competition was assessed for cells grown in LFM (grey bars) or 1M NaCl LFM (magenta bars). Grey lines represent population standard deviation. We used a significance level cutoff of  $P < 0.05$  to determine significant mean amplitude difference compared to BY4741 in competition with itself (mCherry- *versus* EYFP-expressing strains). We determined significant mutant amplitude differences separately for competition in LFM (grey star) or 1M NaCl LFM (magenta star). (C) From 18 phosphosites phosphonull mutant competition assays (light grey), 13 phosphonull mutants showed a fitness effect in either LFM (dark grey circle) and/or 1M NaCl LFM (yellow circle) conditions. Related to Figure 5.

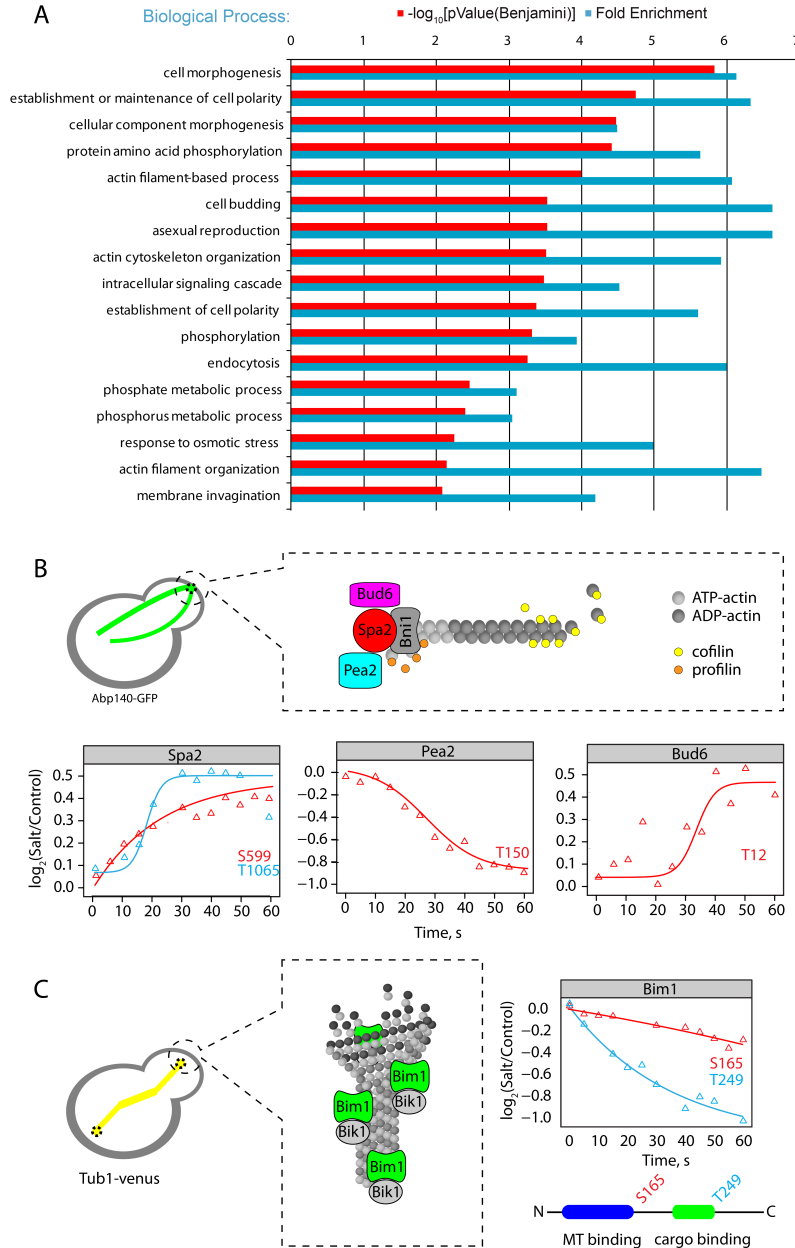


**Figure S6. GO enrichment analysis for differentially regulated phosphoproteins following osmotic shock.** (A) Significantly enriched ( $P<0.01$ ) GO terms among phosphoproteins containing dynamic phosphosites. Gene ontology enrichment analyses were performed with DAVID bioinformatics resources using the entire *S. cerevisiae* proteome as background. In order to eliminate biases of LC-MS/MS workflow (e.g. towards more abundant phosphoproteins) we performed parallel GO analysis of proteins with static phosphosites and removed overrepresented terms from the final figure. (B) Schematics of Abp140-marked actin cables and F-actin regulation at the bud tip by polarisome proteins Spa2, Pea2 and Bud6 with their respective dynamic phosphosites. (C) Schematic of Bim1-driven microtubule integrity following osmotic shock (assessed with Tub1-YFP reporter) and Bim1 dynamic phosphosites on its N-terminal microtubule (MT) binding domain and C-terminal cargo binding EB1 domain. Related to Figure 6.

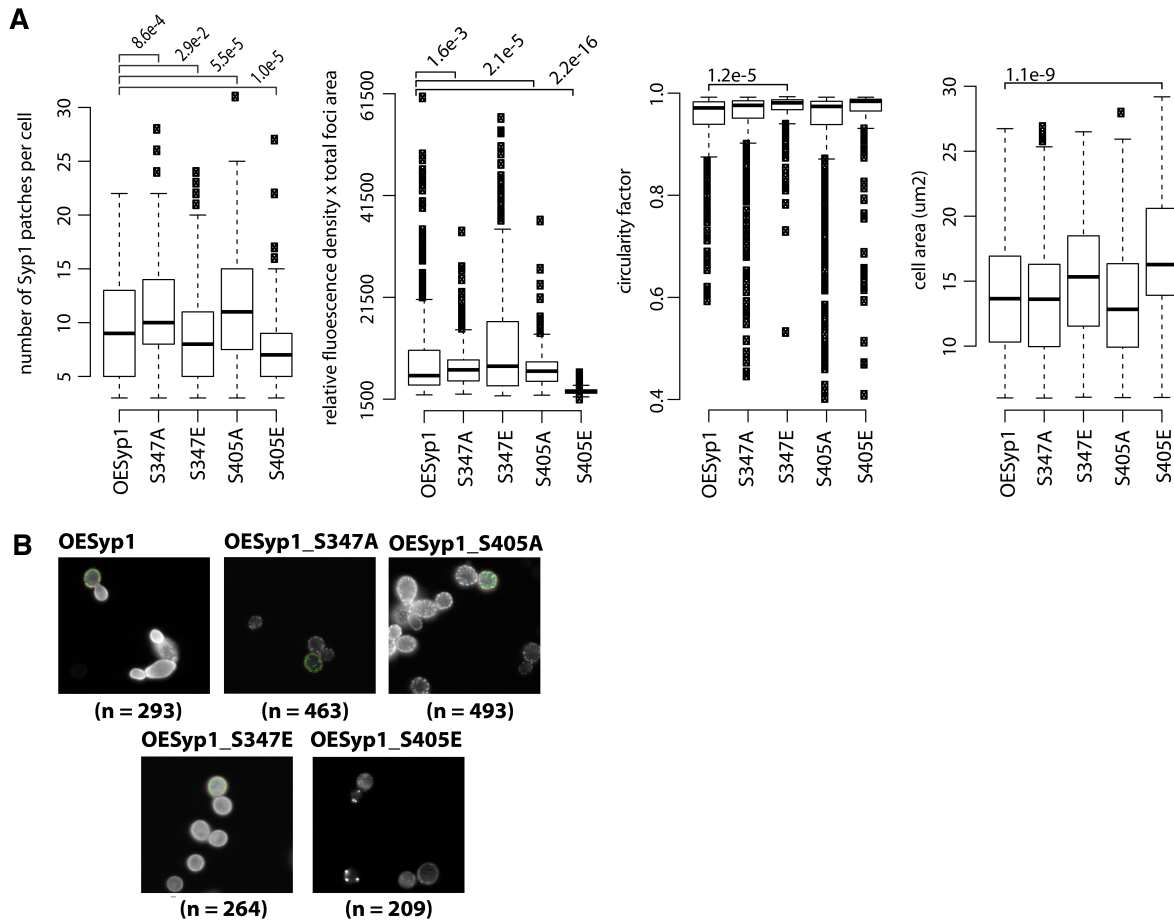


**Figure S7. Characterization of OE Syp1 and S347, S405 mutant strains.** (A) We determined the number of Syp1-GFP marked cortical patches (top left), expression levels of Syp1-GFP defined by the relative fluorescence density per  $\mu\text{m}^2$  (top right), circularity factor (bottom left) and cell size in  $\mu\text{m}^2$  (bottom right) by morphometric and quantitative analysis of segmented cells. T-tests were performed to compare a sampling of 200 cells from OESyp1 to all other strains, *p*-values are indicated if  $< 0.05$ . (B) Bright-field and fluorescence imaging of over expressed (OE) Syp1 constructs in *SYP1* deletion strain with a segmented cell example and respective number of cells analyzed (n) per strain. Related to Figure 7.

## Supplemental Movies

**Movie S1. Time-lapse dynamics and integrity of actin cortical patches under normal condition.** We performed time-lapse fluorescent imaging of cortical patches in BY4741 cells grown in regular low fluorescence medium (LFM). Acquisition times are indicated in the top left corner (frames acquired per minute are displayed at a rate of 1 frame per sec). Cortical patches were monitored with Sla1-GFP and Abp1-mCherry in LFM. Related to Figure 6.

**Movie S2. Time-lapse dynamics and integrity of actin cortical patches under salt condition.** We performed time-lapse fluorescent imaging of cortical patches in BY4741 cells grown in regular low fluorescence medium (LFM) with 0.4 M NaCl. Acquisition times are indicated in the top left corner (frames acquired per minute are displayed at a rate of 1 frame per sec) and presence of NaCl is indicated in the top right corner. Cortical patches were monitored with Sla1-GFP and Abp1-mCherry in LFM with 0.4 M NaCl. Related to Figure 6.

## Supplemental Tables

**Table S1.** Temporal profiles of 5453 phosphopeptides on 1656 proteins with a false discovery rate (FDR) less than 1% at both peptide and protein levels. These profiles correspond to phosphopeptides quantified in at least 10 of 13 time points with a phosphosite localization confidence greater than 0.75. Related to Figure 1.

**Table S2.** We identified 596 dynamic phosphopeptides from 332 proteins that showed distinct continuous changes in phosphorylation with time after salt treatment. We separately listed the kinases and phosphatases that display a dynamic change in phosphorylation within 60 seconds following salt stimulation. Also all dynamic and static profiles were empirically fitted to a birth-extinction model. The maximum rate of fold change in depletion or enrichment ( $dFC/dt_{max}$ ), and the time at which the maximum rate is observed ( $t_{max}$ ) were extracted. Related to Figure 3 and Figure 4.

**Table S3.** MaxQuant “parameters.txt” and “experimentalDesign.txt” files used in this study and kinetic profiles for non-phosphorylated peptides used to model experimental variability in order to estimate thresholds for significant FC ratios of phosphopeptides. Related to Extended experimental procedures.

## Supplemental Files

**File S1.** R environment script and step-by-step instructions to interact with the data and access all dynamic and static temporal profiles. Supplemental file is provided in .zip format. Related to Figure 1.

**File S2.** Clustered protein-protein association matrix to visualize multiple degrees of interactions between dynamic phosphoproteins. Direct and indirect interactions between dynamic phosphoproteins that belong to the same complex can be visualized with iVici software. Related to Figure 6.

## Extended Experimental Procedures

### Terminology

Term	Definition
FC	Fold change in abundance of the corresponding peptide (phosphopeptide) between control and treated (0.4 M NaCl) conditions.
Kinetic profile	Represents phosphorylation dynamics on particular phosphopeptide represented by corresponding FC values measured at all time points.
Amplitude of response	Maximum deviation of the $\log_2(\text{FC})$ from 0. Could be used in the context of individual measurements (single time point) or over the whole kinetic profile.
Regulated phosphosites	Phosphosites with statistically significant amplitude of response at particular time point.
Regulated profile	Kinetic profile showing statistically significant changes in phosphorylation (as defined by FC-based or pattern-based analysis, see below).
Dynamic profile	Regulated profile that was assigned (membership > 0.5) to one of the clusters after c-means clustering.
Dynamic phosphosite	Phosphosite represented by a dynamic profile.
Dynamic protein	Protein that contains at least one dynamic phosphosite.
Static profile	Kinetic profile that is not considered dynamic.
Static phosphosite	Phosphosites represented by a static profile.

### Cell culture

To allow for quantitative SILAC mass spectrometry we used an S288 strain in which genes

encoding *de novo* arginine or lysine synthetic enzymes Argininosuccinate lyase (*ARG4*) and Saccharopine dehydrogenase (*LYS1*) are deleted (S288C *LYS1Δ::kanMX; ARG4Δ::kanMX* strain - a generous gift of Ole Jensen, University of Southern Denmark). Cells were then grown in Synthetic Dextrose (SD) supplemented with either <sup>12</sup>C-, <sup>14</sup>N- (light) or <sup>13</sup>C-, <sup>15</sup>N- (heavy) lysine and arginine (Cambridge Isotope Laboratories). Cells were inoculated into and grown in SD medium (0.17% yeast nitrogen base without amino acids, 0.5% ammonium sulfate, 2% glucose, appropriate amino acids) supplemented with light or heavy arginine (20 mg/L) and lysine (30 mg/L). In order to prevent arginine to proline metabolic conversion, media were also supplemented with L-Proline (20 mg/l). Typically, after 7-9 doublings, heavy culture incorporated almost 100% of heavy arginine and lysine. Cells were grown until late-exponential phase (OD<sub>600</sub>=0.8-1).

#### *Cell stimulations*

All treatments were performed with cultures at OD<sub>600</sub>=1. Light and heavy cultures were split into 25 mL portions. Heavy cultures were treated with 4 M NaCl dissolved in the culture medium (preheated to 30°C) to a final concentration of 0.4 M NaCl. Light cultures were used as controls and were treated with the corresponding volume of culture medium without NaCl. In order to stop all metabolic activity at specific times, individual light and heavy cultures were combined at fixed interval following treatment (0-60 seconds at 5 second intervals) in ~ 500 ml of liquid nitrogen and stored at -80°C.

#### *Cell lysis*

Cells were lysed by mechanical grinding under liquid nitrogen using a Freezer Mill apparatus

(BioSpec). Efficiency of the lysis was monitored by microscopy. Lysis efficiency depends on cell concentration and in our case in order to lyse > 90% of cells, frozen cultures had to be ground for 32 cycles consisting of 2 minute grind at maximum intensity with 2 min cool down periods in between. Frozen culture powders were stored at -80°C.

#### *Protein extraction*

In order to concentrate and purify proteins from other components of culture media, they were precipitated with TCA. Frozen culture powders were mixed with equal volume of 30% TCA solution and incubated on ice for 2 hours. Then samples were centrifuged at 20,000 x g for 20 minutes at 4°C. Supernatants were discarded and protein pellets were washed in 10 mL of cold 10% TCA and centrifuged one more time. Then pellets were washed in cold acetone and proteins were resolubilized in 8 M urea buffer (8 M urea, 100 mM Tris pH 8.0, supplemented with HALT phosphatase inhibitor cocktail (Pierce)). Samples were cleared by centrifugation at 40,000 x g for 10 min, the supernatants were transferred into clean tubes and the protein concentrations were measured by BCA assay (Thermo Fisher Scientific).

#### *Enzymatic digestion*

Disulfide bridges were reduced by adding dithiothreitol to a final concentration of 5 mM and incubating at 56 °C for 30 minutes. The samples were allowed to cool down to room temperature and the reduced cysteines were alkylated by adding iodoacetamide to 15 mM and incubating for 30 minutes in the dark at room temperature. Alkylation was quenched with 5 mM dithiothreitol and incubation for an additional 15 minutes. Samples were diluted 6 times with 20 mM TRIS pH 8 containing 1 mM CaCl<sub>2</sub> and trypsin was added to an enzyme to substrate mass ratio of 1:50.

Proteins were digested overnight at 37°C. Because trypsin cleaves after arginine or lysine, heavy and light versions of every peptide (except the very C-terminal peptide of each protein) should be distinguishable based upon the mass difference between the heavy and light versions of at least one lysine or arginine. After digestion peptide mixtures were acidified by addition of FA to a final concentration of 1%, clarified by centrifugation (20,000 x g 10 min) and desalted on Oasis HLB cartridges (Waters) according to the manufacturer instructions. Peptide eluates were snap-frozen in liquid nitrogen, lyophilized in a speedvac and stored at -80°C.

#### *Phosphopeptide isolation*

Tryptic digests were subjected to the TiO<sub>2</sub> enrichment protocol as described previously (Kanshin et al., 2013). Briefly, sample loading, washing, and elution steps were performed in homemade spin columns assembled following the StageTip extraction (Ishihama et al., 2006; Rappaport et al., 2003) and comprised of 200 μL pipette tip with frit made of SDB-XC membrane (3M) and filled with TiO<sub>2</sub> beads. SDB-XC material has similar hydrophobic properties as C18 and allows for combining phosphopeptide enrichment and desalting steps. Centrifugation speed was set to 2,000 x g. Before peptide loading, columns were equilibrated with 100 μl of loading buffer (250 mM lactic acid in 70% ACN 3% TFA). Peptides were solubilized in 100 μL of loading buffer and applied on a TiO<sub>2</sub> column. Each column was washed with 100 μL of loading buffer followed by 2 x 100 μl of 125 mM asparagine and glutamine in 70% ACN 3% TFA and 100 μl of 70% ACN 3% TFA. Subsequent washing with 50 μl of 1% FA was used to equilibrate SDB-XC frit material. Phosphopeptides were eluted from TiO<sub>2</sub> with 2 x 50 μL portions of 500 mM Na<sub>2</sub>HPO<sub>4</sub> pH 7 and retained on SDB-XC. Peptides were desalted in 50 μL of 1% FA and subsequently eluted from SDB-XC in 50 μl of 50% ACN 0.5% FA. Eluates were dried on a speedvac and

stored at -80°C.

#### *Off-line fractionation of phosphopeptides*

In order to increase phosphoproteome coverage prior to MS analysis, phosphopeptides were fractionated offline by SCX chromatography. Peptides were solubilized in 100  $\mu$ L of loading buffer (0.2% FA 15% ACN) and loaded onto StageTips containing 6 mg of Poly-sulfoethyl-A SCX phase. Then columns were washed with an additional 50  $\mu$ l of the loading buffer and peptides were eluted in 100  $\mu$ L salt steps with 40, 70, 100, 150 and 500 mM NaCl dissolved in loading buffer. Flow-through and salt fractions were dried on a speedvac, resuspended in 15  $\mu$ L of 4% FA and analyzed by nanoLC-MS/MS.

#### *nanoLC- MS/MS*

SCX fractions obtained after offline fractionation were analyzed by online reverse phase chromatography coupled with an electrospray ionization interface to acquire MS (measuring intensity and m/z ratio for peptides) and MS/MS (fragmentation spectra of peptides) scans. A nanoflow HPLC system (Eksigent, Thermo Fisher Scientific) was used for online reversed-phase chromatographic separation; peptides were concentrated on 5 mm long trap columns (inner diameter 300  $\mu$ m) and separated on 18 mm long fused silica capillary analytical columns (inner diameter 150  $\mu$ m), both packed with 3um 200A Magic AQ C18 reverse-phase material. Peptides were eluted by an increasing concentration of buffer B (5-40% in 100 min). Following the gradient elution, the column was washed with 80% buffer B and re-equilibrated with 5% buffer B. The HPLC solvent A was 0.2% FA and the solvent B was ACN/0.2% FA. Peptides were eluted into the mass spectrometer at a flow rate of 600 nL/min. The total run time was

approximately 125 min, including sample loading and column conditioning. Peptides were analyzed using an automated data-dependent acquisition on a LTQ-Orbitrap Elite mass spectrometer. Each MS scan was acquired at a resolution of 240,000 full width half maximum (at 400 m/z) for mass range m/z 300-2,000 with the lock mass option enabled (m/z: 445.120025) and was followed by up to 12 MS/MS data dependent scans on the most intense ions using collision induced dissociation (CID). AGC target values for MS and MS/MS scans were set to 1e6 (max fill time 500 ms) and 1e5 (max fill time 50 ms) respectively. The precursor isolation window was set to 2 m/z with CID normalized collision energy of 35, the dynamic exclusion time was set to 60 s.

#### *MS Data processing and analysis*

MS data were analyzed using MaxQuant (Cox and Mann, 2008; Cox et al., 2011b) software version 1.3.0.3 and searched against the SGD database (<http://www.yeastgenome.org/>) containing 5,904 entries. A list of 248 common laboratory contaminants included in MaxQuant were also added to the database as well as reversed versions of all sequences. For searching, the enzyme specificity was set to trypsin with the maximum number of missed cleavages set to 2. The precursor mass tolerance was set to 20 ppm for the first search (used for non-linear mass recalibration (Cox et al., 2011a)) and then to 6 ppm for the main search. Phosphorylation of serine, threonine and tyrosine residues was searched as variable modification; carbamidomethylation of cysteines was searched as a fixed modification. The false discovery rate (FDR) for peptide, protein, and site identification was set to 1%, the minimum peptide length was set to 6, and the filter ‘labeled amino acid’, and ‘peptide requantification’ functions were enabled. To match identifications across different conditions, the ‘match between runs’ option in MaxQuant was

enabled with a retention time window of one minute. MaxQuant parameters.txt and experimentalDesign.txt files used in this study are listed in Table S3.

#### *Data quality filtering*

In addition to FDR, which was set to a maximum of 1% for peptide, protein and phosphosite identification levels, we used some additional criteria to increase data quality. First we considered only peptides for which isotopic abundance ratios ( $FC=Salt/Control$ ) were measured in at least 10 time points (out of 13). Thus all kinetic profiles are represented by at least 10 points. Then we set a cut-off for phosphosite localization confidence across experiments (time points) to 0.75. Based on these criteria we obtained 5453 high confidence phosphosite kinetic profiles (Table S1). To demonstrate the reproducibility of the results we included preliminary data obtained at a lower temporal resolution and with fewer identified pSites due to LC-MS/MS setup (1DLC and short gradients) (Figure S1E). pSites detected in both studies showed qualitatively similar temporal profiles (Figure S1G). We plotted FC ratios obtained in 2 studies against each other for each pSite and calculated the slope and  $R^2$  of the corresponding correlation as measures of similarity (Figure S1E-F).

#### *Accessing significance of phosphosites*

As in any large-scale phosphoproteomics experiment, the majority of detected phosphopeptides are not affected by the treatment. It is thus required to choose regulated phosphosites prior to subsequent analysis. The standard approach to define regulated sites is based on the value of the fold change (FC) ratio between conditions, e.g. it is often considered that peptides that are either up-regulated ( $FC=2$ ) or down-regulated ( $FC=1/2$ ) by 2 fold have undergone significant changes.

Since phosphopeptide enrichment selectivity in our experiment was lower than 100%, we also had kinetic profiles for non-phosphorylated peptides (Table S3) that were not supposed to be affected by any short treatments (we assume that there are no significant changes in protein abundance taking place within 1 min). We used these FC ratios as a true-negative distribution in order to estimate what are significant FC ratios for phosphopeptides ( $P < 0.05$  with correction for multiple hypothesis testing). The major limitation of this approach is that phosphosites with low FC ratios can be eliminated. The dynamic nature of our dataset allowed us to apply a complementary method that does not consider values of FC but rather relies on the continuity of consecutive data points in a dynamic trace. The approach has been applied to the analysis of gene expression profiles (Willbrand et al., 2005) but is applicable to any kind of temporal data analysis with a sufficient number of measurements ( $>10$ ). In our case, a kinetic profile was transformed into a pattern signature based on the difference between adjacent FC values (Figure 1E). We identified non-random time traces by using the correlation between random data and the probability  $P(\sigma)$  of a trace up–down signature (Figure 1E). By assumption, most profiles are not correlated with the independent time variable and hence will exhibit random fluctuations. The small number of profiles that are correlated will tend to exhibit more regular behavior. Briefly, the equivalence between up–down properties of random data and the up–down properties of random permutations allowed us to calculate the probability  $P(\sigma)$  that a random trace has signature  $\sigma$  of length  $N$ .

The probability  $P(\sigma)$  that  $N + 1$  random time points has a signature  $\sigma$  is :

$$P(\sigma) = \frac{C(\sigma)}{(N+1)!}$$

Thus a dynamic profile with signature  $\sigma$  is correlated with the independent time variable by the probability  $A(\sigma, M)$ . The probability that all of  $M$  random signatures have frequency greater than  $C(\sigma)$  is given by:

$$A(\sigma, M) = F(\sigma) \cdot M$$

We decided to use an  $A(\sigma, M)$  cutoff of 0.9, in which  $1/[1-A(\sigma, M)]$  represents the number of times one has to repeat a random experiment to find a profile with signature as unlikely as  $\sigma$ . We used both FC-based and pattern-based analyses to obtain a list of regulated profiles. A kinetic profile was considered to be regulated if it had either more than 3 significant FC ratios (621 profile) or if the probability of getting even a single profile in the dataset by chance was lower than 0.1 (345 profiles) (Figures S1C-D). Interestingly pattern-based analysis allowed us to identify 116 significant kinetic profiles, of which 99 were uniquely discovered in pattern-based analysis, some having very low FC ratios that would have remained undetected by standard FC-based approach (Table S2).

#### *Fitting of dynamic profiles*

We modeled the phosphosite kinetic profiles with non-linear regression using the Matlab fit type function with the following birth-death model:

$$FC(t) = \left(1 - \frac{c}{\exp\left(\frac{t-d}{a}\right)+1}\right) + b$$

where  $t$  is time,  $FC(t)$  is the fold change ratio between conditions ( $FC=Salt/Control$ ) and the

kinetic profile-specific constants starting values were set to  $a = 0.219$ ,  $b = 0.308$ ,  $c = 0.711$  and  $d = 0.571$ .

We performed a first derivative test to determine the local maximum or minimum rate of change ( $dFC/dt$ ) of the phosphosite kinetic profiles (Figure 3C and Figure S3A) and also extracted the time at which the maximum absolute rate is observed ( $dFC/dt_{max}$ ) (Figure 3C). Fits and values extracted from first derivative are available in Table S2. We applied simple statistics to determine the mean, standard deviation and excess kurtosis ( $\mu^4/\sigma^4 - 3$ ) of the distribution on a  $\log_{10}$  scale of  $dFC/dt$  for the dynamic profiles. This analysis confirmed that the distribution of  $dFC/dt|_{max}$  of dynamic profiles is leptokurtic (kurtosis value of 1.03) compared to the normal distribution with a more acute peak around the mean and fatter tails. This observation is complemented by the fact that 98.5% of the dynamic profile rates are distributed within 2 orders of magnitude ( $+/- 2$  SD from the mean) or 68.3% within about 1 order of magnitude ( $+/- 1$  SD).

Next, we interpreted the shapes of the fitted profiles by calculating the second derivative of the birth-death model (Figure 3C). The values and difference between local max and min of the second derivative within the time range of measurements (0 to 60 seconds) allowed us to classify dynamic profiles into: (i) sigmoid-like traces with a positive max and negative min, (ii) exponential-like traces displaying max and min values in the same Cartesian quadrant and (iii), linear-like traces having a difference between max and min smaller than 4e-05 (Figure S3B). The max and min difference cutoff for linear-like shape classification was determined with the distribution of the second derivative difference of all of the dynamic profiles (Figure S3B).

#### *Clustering of kinetic profiles, GO and PPI network analysis*

All regulated kinetic profiles were used for "soft" clustering (Futschik and Carlisle, 2005) which

offers several advantages compared to "hard" clustering methods. First, it indicates how well corresponding clusters represent temporal profiles. Second, the overall relation between clusters, and thus a global clustering structure, can be defined. Additionally, soft clustering is more robust to noise. We used fuzzy C-means algorithm (Nock and Nielsen, 2006). Analysis and visualization were performed in the R environment (<http://www.r-project.org/>) with the Mfuzz package (Kumar and Futschik, 2007). Optimal setting of the "fuzzifier" parameter was 1.242 as estimated with the mestimate function. In order to find the optimal number of clusters, we performed repeated soft clustering for a range of cluster numbers from 2 to 20 and calculated the minimum centroid distance (minimum distance between two cluster centers produced by c-means clustering) (Schwammle and Jensen, 2010). Based on this analysis we chose to use 6 clusters. All regulated (both pattern and FC-based analysis) profiles (737) were used for clustering which resulted in 596 profiles belonging to 332 proteins being assigned to one of the clusters with membership value higher than 0.5. These sites were considered "dynamic" (Table S2). It has to be noted that there still could be biologically regulated phosphosites that were not selected by our filtering procedure. Particularly it could be low-abundance phosphosites for which precise quantification is more difficult due to low intensity of the signal. Thus corresponding kinetic profiles could be masked by technical MS noise.

Gene ontology enrichment analyses were performed in DAVID bioinformatics resources (Huang da et al., 2009a, b) for proteins containing dynamic phosphosites against whole *S. cerevisiae* proteome as background. In order to eliminate GO terms that could be enriched due to the nature of our experiment (e.g. MS detection can be biased towards high abundant proteins) we performed parallel GO analysis for proteins containing only static phosphosites and then subtracted the results from our initial analysis. We thus treat enrichment in the static data set as

background.

A protein-protein interaction network was built in STRING for all proteins containing dynamic phosphosites (Franceschini et al., 2013). All interaction predictions were based on experimental methods with the minimal confidence score of 0.9. Results were visualized in Cytoscape network visualization and analysis (Cline et al., 2007; Shannon et al., 2003; Smoot et al., 2011). Alternatively, we clustered the dynamic phosphoproteins using an association matrix based on the number of links that connect two proteins, described in (Tarassov et al., 2008). This approach also allows visualizing non-direct interactions between proteins that belong to the same complex. Briefly, the interaction network was retrieved from Biogrid (Breitkreutz et al., 2003; Chatr-Aryamontri et al., 2013) and organized into an association matrix with entries for pairs of dynamic phosphoproteins that range between 0 and 1. Values were calculated as  $1/d_2$ , where  $d$  is the shortest path in the network between these two proteins. A hierarchical agglomerative average linkage clustering with the uncentered correlation coefficient as the distance matrix was then applied to the association matrix. We visualized these interactions using iVici (<http://michnick.bcm.umontreal.ca/ivici/>) (Tarassov et al., 2008).

We performed kinase prediction for our dynamic phosphosites (60 sec) as well as those affected after 5 and 20 min upon osmotic stress using PhosphoSiteAnalyzer Software (Bennetzen et al., 2012) based on NetworKIN algorithm (Linding et al., 2008) and we used MotifX (Chou and Schwartz, 2011; Schwartz and Gygi, 2005) to look for over represented linear motifs in our data. We used default settings (min. occurrences = 20, significance = 0.000001) and whole yeast proteome as background.

### *Rates of evolution of phosphosites*

Rates of evolution were determined for all phosphosites as described previously by Landry et al. (Landry et al., 2009). The analysis was performed on the subset of peptides that were monophosphorylated. We considered phosphosites in both ordered and disordered protein regions. We determined a significant difference in distribution of rates of evolution ( $p$ -value = 0.0014) with a Kolmogorov-Smirnov test between the dynamic and static sites. No significant difference in rates of evolution ( $P$ -value = 0.3420) was observed between a literature-curated set of functional phosphosites (Beltrao et al., 2012) and our dynamic set of phosphosites.

### *Site-directed mutagenesis*

To examine the fitness effects of dynamic and static phosphosites on Hog1, Rck2, Gpd1, Bud6, Bim1, Syp1 and Sla1 and the potential functions of Syp1 dynamic phosphosites Ser347 and Ser405, we created phosphomimetic (Ser-Glu) and/or phospho-null (Ser-Ala; Thr-Ala; Tyr-Ala) mutants of these residues. Disruption of dynamic phosphosites was achieved using a standard site-directed mutagenesis protocol with the high fidelity AccuPrime DNA polymerase (Invitrogen) and DpnI restriction enzyme (NEB). Gene-specific primers for site-directed mutagenesis were designed using Primer-BLAST online software (Ye et al., 2012) and mutations were performed on either MoBY-ORF plasmids for Hog1, Rck2, Gpd1, Bud6, Bim1, Syp1 and Sla1 genes (Ho et al., 2009) or the budding yeast ORF collection BG1805 vector (Open Biosystems) containing the Syp1 gene. We used distinct mutagenic primer pairs to generate the mutants listed below. All ORF mutations were confirmed by sequencing.

Phospho-null mutants of MoBY-ORF plasmids were used as is with their wild type counterparts in the competition growth assays (see below). Mutated Syp1 sequences in BG1805 were then

cloned into the Gateway destination vectors pAG406GPD-ccdB and/or pAG416GPD-ccdB-EGFP using Gateway cloning technology (Invitrogen). These Syp1-encoding plasmids were transformed into the BY4741 cellular background and integrants were selected in uracil-depleted medium and final clones were confirmed by sequencing. Constructs in pAG406GPD vector allowed genome integrated expression of coding sequences in BY4741 Sla1-GFP Abp1-mCherry cells whereas constructs in pAG416GPD-EGFP were expressed from plasmids in BY4741 *SYP1Δ* cells.

*Yeast strains used in this study and mutagenic primer pairs to generate all phosphosite mutants.*

Strain	ORF	vector	mutation	primer pair used for site-directed mutagenesis	background	co-vector
YPH499	NA	NA	NA	NA	S288C LYS1Δ::kanMX; ARG4Δ::kanMX	NA
BY4741 ABP1-mCherry SLA1-GFP	NA	NA	NA	NA	BY4741 ABP1-mCherry::NAT1 SLA1-GFP::HPt	NA
BY4741 TUB1-YFP	NA	NA	NA	NA	BY4741 TUB1-YFP::HPt	NA
BY4741 ABP140-GFP	NA	NA	NA	NA	BY4741 ABP140-GFP::HPt	NA
BY4741 SYP1-YFP	NA	NA	NA	NA	BY4741 SYP1-YFP::HPt	NA
BY4741 EYFP	NA	NA	NA	NA	MATa his3Δ1 leu2Δ0 met15Δ0 ura3Δ0	p413ADH1-EYFP
BY4741 mCHERRY	NA	NA	NA	NA	MATa his3Δ1 leu2Δ0 met15Δ0 ura3Δ0	p413ADH1-mCherry
HOG1 <i>wildtype</i>	HOG1	p5472	NA	NA	BY4741 HOG1Δ::kanMX	p413ADH1-EYFP
RCK2 <i>wildtype</i>	RCK2	p5472	NA	NA	BY4741 RCK2Δ::kanMX	p413ADH1-EYFP
GPD1 <i>wildtype</i>	GPD1	p5472	NA	NA	BY4741 GPD1Δ::kanMX	p413ADH1-EYFP
SYP1 <i>wildtype</i>	SYP1	p5472	NA	NA	BY4741 SYP1Δ::kanMX	p413ADH1-EYFP
BIM1 <i>wildtype</i>	BIM1	p5472	NA	NA	BY4741 BIM1Δ::kanMX	p413ADH1-EYFP
SLA1 <i>wildtype</i>	SLA1	p5472	NA	NA	BY4741 SLA1Δ::kanMX	p413ADH1-EYFP
BUD6 <i>wildtype</i>	BUD6	p5473	NA	NA	BY4741 BUD6Δ::kanMX	p413ADH1-EYFP
HOG1_T174A	HOG1	p5472	T174A	GAATTCAAGACCCCTAAATGGCTGGCTATGTTCCACTAGATAC GTATCTAGTGGAAACATAGGCCAGCCTTGAGGGCTTGAATT	BY4741 SYP1Δ::kanMX	p413ADH1-mCherry
HOG1_Y176A	HOG1	p5472	Y176A	CAAGACCCCTCAAATGACAGGCCTGTTCCACTAGATACTACAG CTGTAGTATCTAGTGGAAACAGCGCCTGTCAATTGAGGGCTTG	BY4741 SYP1Δ::kanMX	p413ADH1-mCherry
RCK2_T379A	RCK2	p5472	T379A	CCAAGAACACCAAGGCCTTGTGGTACAG CTGTACACACAAGGAGCCTGGTCTTGG	BY4741 SYP1Δ::kanMX	p413ADH1-mCherry
GPD1_S24A	GPD1	p5472	S24A	GGTAGAAAAGAGAAGTCCGTTCTGTTGAAGGCTGCCGAAAG GCCTTCAAAGAACAGAACGCGAACCTCTCTTCTACC	BY4741 SYP1Δ::kanMX	p413ADH1-mCherry
GPD1_S27A	GPD1	p5472	S27A	GAGAAGTTCTCTTGTGTTGAAGGCTGCCGAAAG CTTTCGGCAGCCTCAAAGCAACAGAACGAGGAACCTCTC	BY4741 SYP1Δ::kanMX	p413ADH1-mCherry

Strain	ORF	vector	mutation	primer pair used for site-directed mutagenesis	background	co-vector
SYP1_S297A	SYP1	p5472	S297A	CCACAAAAGGATAAGCGTAAGGCTGCATTGGAAACATTGGAC GTCCAATGTTCCAATGCAGCCTTACGCTTATCCTTTGTGG	BY4741 SYP1Δ::kanMX	p413ADH1-mCherry
SYP1_S577A	SYP1	p5472	S577A	CACACTCCTCTCAGATTGCTGGCGAGCTAAGAGAAC GTTCTCTTAGCTCGCCAGCAATCTGAGAGGAGAGTGTG	BY4741 SYP1Δ::kanMX	p413ADH1-mCherry
SYP1_S347A	SYP1	p5472	S347A	CCCTAAGATCTAAAGTGGCGCTATTCGGTAGAAATAAGACC GGTCTTATTCTACCGAAAATAGGCCCACTTAGATCTTAGGG	BY4741 SYP1Δ::kanMX	p413ADH1-mCherry
SYP1_S405A	SYP1	p5472	S405A	CCACCTATTCATCATCAAAGCTAACATTGGACCCGGGTG CACCCGGGGTCCAATTGTTAGCTTTGATGATGAATAGGTGG	BY4741 SYP1Δ::kanMX	p413ADH1-mCherry
BIM1_S165A	BIM1	p5472	S165A	GAGGATTAGCAACAAGACATGCTCGCTGGAAATAACGG CCGTTTATTCCAGCGAAGCATGCTTGTGCTAACCTC	BY4741 SYP1Δ::kanMX	p413ADH1-mCherry
BIM1_T249A	BIM1	p5472	T249A	GAAGGTGTTATAAATTAAATGATGAGGCTATCACCAGGATGGAAATGGGG CCCCATTCCATTACCATGGCGGTGATGCCATCATTAATTATAAACACCTTC	BY4741 SYP1Δ::kanMX	p413ADH1-mCherry
SLA1_S996A	SLA1	p5472	S996A	GGATTAATTCAGCTAACTGGTTCGCTATGCCACTGTACAAAGAACAGCGGC GCCGCTGTTCTTGACAGTTGCATAGCGACACCAGTATTAGCTGAAATTAAATCC	BY4741 SYP1Δ::kanMX	p413ADH1-mCherry
SLA1_T993A	SLA1	p5472	T993A	GGATTAATTCAGCTAACTGGTTCGCTCAATGCCAAC GTTGGCATTGAGACACCAGCATTAGCTGAAATTAAATCC	BY4741 SYP1Δ::kanMX	p413ADH1-mCherry
SLA1_S340A	SLA1	p5472	S340A	GGTGAATATAAAGGTGCTGCTGATCCTGGTTGAGAG CTCTCAACCCAGGATCACGAGCAGCACCTTATTCACC	BY4741 SYP1Δ::kanMX	p413ADH1-mCherry
SLA1_S437A	SLA1	p5472	S437A	CAAGAAAAACTTCACCAAAAGCTCCATCTAGGTGAGATC GATCTGACCTAGATGGAGCTTGGTAAGTTTCTTG	BY4741 SYP1Δ::kanMX	p413ADH1-mCherry
SLA1_T818A	SLA1	p5472	T818A	CTAAAAAGGAGCTGCCCTCGGCTCTGAACCAAACCTAAAAG CTTTAGTTGGTTAGGAGCCGAGGCAGCTGCCCTTTAG	BY4741 SYP1Δ::kanMX	p413ADH1-mCherry
BUD6_T12A	BUD6	p5472	T12A	GTGGATGACCCCTACGTATGGCGCTCAAAGATTAAGAACACTGC GCAGTTTTAATCTTGAGGCCATACGTAGGGTCATCCAC	BY4741 SYP1Δ::kanMX	p413ADH1-mCherry
BUD6_S233A	BUD6	p5472	S233A	CAATGCTCAAACGCAAGCTGATGATGATGATGC GCATCATCATCATCAGCTCGTTGGAGCATTG	BY4741 SYP1Δ::kanMX	p413ADH1-mCherry
OESYP1-EGFP	SYP1	pAG416GPD-EGFP	NA	NA	BY4741 SYP1Δ::kanMX	NA
OESYP1_S347A-EGFP	SYP1	pAG416GPD-EGFP	S347A	CCCTAAGATCTAAAGTGGCGCTATTCGGTAGAAATAAGACC GGTCTTATTCTACCGAAAATTCGCCACTTAGATCTTAGGG	BY4741 SYP1Δ::kanMX	NA
OESYP1_S347E-EGFP	SYP1	pAG416GPD-EGFP	S347E	CCCTAAGATCTAAAGTGGCGAAATTTCGGTAGAAATAAGAC GTCTTATTCTACCGAAAATTCGCCACTTAGATCTTAGGG	BY4741 SYP1Δ::kanMX	NA
OESYP1_S405A-EGFP	SYP1	pAG416GPD-EGFP	S405A	CCACCTATTATCATCAAAAGCTAACAAATTGGACCCGGGTG CACCCGGGGTCCAATTGTTAGCTTTGATGATGAATAGGTGG	BY4741 SYP1Δ::kanMX	NA
OESYP1_S405E-EGFP	SYP1	pAG416GPD-EGFP	S405E	CCCACCTATTATCATCAAAAGAAAACAATTGGACCCGGGTG CACCCGGGGTCCAATTGTTCTTTGATGATGAATAGGTGG	BY4741 SYP1Δ::kanMX	NA
OESYP1	SYP1	pAG406GPD	NA	NA	BY4741 SYP1Δ::kanMX	NA
OESYP1_S405E	SYP1	pAG406GPD	S405E	CCCACCTATTATCATCAAAAGAAAACAATTGGACCCGGGTG CACCCGGGGTCCAATTGTTCTTTGATGATGAATAGGTGG	BY4741 ABP1-mCherry::NAT1 SLA1-GFP::HPt	NA

### *Assessment of phospho-null mutant fitness through competition-growth*

Target phosphosites were selected amongst dynamic proteins involved in the main HOG response and complementary actin and tubulin cytoskeletal responses. We successfully generated 18 phospho-null mutants on 7 proteins that showed a fitness defect under salt conditions when deleted. Our set of phospho-null mutant phosphosites consisted of 13 dynamic and 5 static pSites. Phospho-null mutants were expressed from MoBY-ORF p5472 plasmids and we measured their performance to complement their respective deletion strains. We considered only dynamic and static phosphosites with rates of evolution below 1.8 (Landry et al., 2009).

Each phospho-null mutant strain was also transformed with a p413 plasmid coding for mCherry monomeric RFP and the wild type strains with a p413 plasmid coding for EYFP. Both fluorescent reporters were expressed under the control of a constitutive *ADH1* promoter. Competent cells of respective deletion strains were co-transformed with the specific mutant or wild type ORF and fluorescent marker expression plasmid combinations and co-integrants were selected in uracil-histidine-depleted medium supplemented with geneticin.

To assess fitness of phospho-null mutants in competition growth, the mutants and their corresponding wild type protein-expressing strains were cultured together starting from OD<sub>600</sub> of 0.5 and mixed in equal quantities, diluted 1:100 and grown in competition at 30°C for 5 days in normal LFM or LFM supplemented with 1M NaCl. Cells were diluted 1:50 once or twice per day to keep them in exponential growth. OD<sub>600</sub> of cultures were monitored with an automated Spectra MAX 190 microplate spectrophotometer (Molecular Devices). Fluorescence of each population in competition was monitored every 8 to 16 hours with a SpectraMax Gemini XS microplate reader spectrophotometer (Molecular Devices). Absorbance and fluorescent emissions were acquired on samples dispensed in special optics 96-well plates (Corning Costar

3614). Fluorescent acquisitions for the EYFP channel were conducted with excitation fixed at 485 nm and emission at 535 nm, whereas acquisitions on the RFP channel were conducted with excitation at 570 nm and emission at 620 nm.

Analyses were performed in the R environment, respective mCherry and EYFP relative fluorescent units were normalized and trends in population fraction changes were fitted to a bounded exponential equation (Figure S5). To determine the amplitude of single population fraction changes, we subtracted the initial value (0.5) from the respective time-point values. To determine a change in population fraction we calculated the respective amplitude mean for the concatenated time points 24 hours to 120 hours ( $n = 72$ ) and we used control strain BY4741 mixed in competition with itself to perform a Welch's t-test with a significance level cutoff of  $P < 0.05$  (Figure S5B-C). With this approach we calculated that a proportion of 0.72 (13 out of 18) phospho-null mutants showed a fitness effect with a statistical significance of  $P = 0.0481$  (binomial test).

#### *Fluorescent protein-tagged reporter strains*

All strains for visualizing actin cortical patches, actin cables and microtubules contained cellular coding sequences for fluorescent proteins integrated into the genome 3' to reporter protein ORFs. The fluorescent tags where integrated by homologous recombination as described previously (Tarassov et al., 2008). GFP constructs (Sla1-GFP and Abp140-GFP) were a generous gift from J Vogel at McGill University. Abp1-mCherry, Tub1-Venus and Syp1-Venus were tagged via homologous recombination by amplifying the HPH resistance cassette from pAG32-mCherry or pAG32-Venus YFP (yellow fluorescent protein variant) (Malleshaiah et al., 2010) with primer tails with homology to flanking sequences to the *ABP1*, *TUB1* or *SYP1* loci respectively.

BY4741 strain was transformed with the respective PCR cassettes, selected for HPH resistance and confirmed by diagnostic PCR.

### *Microscopy*

For experiments in Figures 6C-F, 7E (left panels) and Movies S1-S2 we used the microfluidic ONIX platform with Y04C plates (Cellasic). Cells were grown in low fluorescent medium (LFM) (Sheff and Thorn, 2004) to an OD<sub>600</sub> of 0.6 and were diluted 1:3 before loading into the chambers. Salt treatment was performed in LFM with 0.4 M NaCl under continuous stable pressure of 5 psi. Fluorescent images were acquired with a Cool SNAP HQ camera on a Nikon TE2000 inverted microscope equipped with a 100X/1.45 plan APO lambda oil objective (Nikon) and respective FITC (Chroma 41001HQ), EYFP (Chroma 49003ET) and mCH/TR (Chroma 49008ET) dichroic cubes. Time course images were acquired for 5-30 min with a continuous flow of LFM or LFM plus 0.4 M NaCl into the immobilization chambers. Two color images were collected sequentially from a single focal plane at frames rates of 5s for Abp140-GFP, Sla1-GFP and Abp1-mCherry, 30s for Syp1-venus YFP and 60s for Tub1-venus YFP. Image analysis and processing of movies and kymographs was performed with NIS elements (Nikon). Alternatively, for experiments in Figures 7B, 7C, 7E and Figure S7 concanavalin A (Sigma-Aldrich ConA # C-2631) was used as a binding agent for imaging on glass bottom 96 well plates (Matrical Bioscience MGB096-1-2-LG-L). Each well was loaded with 0.1% of ConA solution at room temperature for 15 minutes. ConA was removed and wells were washed with sterile water. ConA was activated with 20 mM CaCl<sub>2</sub> and 20 mM MnSO<sub>4</sub> solution and incubated for 15 min at room temperature and washed once again with sterile water. Cells were grown in complete LFM to an OD<sub>600</sub> of 0.6, diluted 1:5 into wells and incubated for 10 min at room temperature allowing

for cells attachment. Images were collected on an InCell 6000 automated confocal microscope configured with a 100x/0.9 Plan FLUOR objective (Nikon) and 488 nm laser diode and FITC 525/20 emission filter for GFP fluorescence (Syp1-EGFP and Sla1-GFP) or 561 nm DPSS laser and dsRed 605/52 emission filter (GE healthcare life sciences) for Abp1-mCherry. Two color images were collected sequentially on a single focal plane with an exposure time of 100 ms and a confocal slit of 2AU. The temperature was maintained at 30 °C.

Image analysis was performed with InCell Developer (GE healthcare life sciences). We used automated cell and Syp1 vesicle top-hat segmentation on phase-contrast and GFP images respectively to define objects for morphometric measurements and quantification of fluorescence. For each strain we concatenated the segmented cells and their linked vesicles from 9 fields of view. Sample cell counts for each mutant strain were as follows: OESyp1 ( $n = 293$  cells), S347A ( $n = 463$  cells), S347E ( $n = 264$  cells), S405A ( $n = 493$  cells) and S405E ( $n = 209$  cells) mutant strains in *SYP1Δ* background and OESyp1 S405A ( $n = 438$  cells) in the wild type (*SYP1* locus intact) background. From these objects, we extracted the Syp1 vesicle count per cell, the cell and vesicle area ( $\mu\text{m}^2$ ), the cell form factor which estimates circularity, and length ( $\mu\text{m}$ ) of the cell longer and shorter perpendicular axes of symmetry to calculate the cell elongation factor. As the GFP signal was limited to Syp1 patches and membrane considered as segmented vesicles, we extracted the integrated density in each vesicle and calculated the level of relative fluorescence per cell. Specifically, for each cell we determined the total integrated density multiplied by vesicle area and corrected for background by subtracting mean fluorescence of background multiplied by total vesicle area. We performed a two-sample t-test to determine if the extracted measurements differed between the Syp1 and all other mutant strains.

A random sampling of 200 cells from each strain allowed the pairwise analysis with a significance level cutoff of  $P < 0.05$ .

## Supplemental Results

### *Identification of putative phosphosites that regulate actin structures and microtubules*

We identified dynamic phosphorylation in protein complexes involved in processes mediated by actin cytoskeleton, including the polarisome and clathrin-mediated endocytosis (CME) (Chowdhury et al., 1992; Reiter et al., 2012). The majority of the sites that we detected have not been reported previously. We did, however, detect a few that are known to have regulatory functions. For example, we detected polarisome protein phosphorylation changes, including of Bud6, which stimulates processive F-actin assembly by the formin Bni1, and the polarity scaffold protein Spa2, which is required for Bni1 localization (Figure S6B) (Moseley and Goode, 2005). Interestingly, we did not observe changes in proteins directly involved in actin cable assembly or degradation, including formins, cofilins or profilins, but only in regulators of F-actin assembly (actin-binding proteins Ysc84 and Abp1) and Arp2/3 dependent branching (WASP homolog Las17, WASP-binding protein Lsb3 and verprolin protein Vrp1).

We also observed dynamic phosphorylation of several proteins involved in mitotic spindle assembly, dynamics and checkpoints, including the Tid3 subunit of the kinetochore Ndc80 complex involved in microtubule attachment and spindle checkpoint activities (McCleland et al., 2003), the Clb3 cyclin that regulates M phase cell cycle progression (Richardson et al., 1992)

and microtubule-associated proteins Mhp1, Stu2 and Bim1, all implicated in microtubule stability and spindle function (Al-Bassam et al., 2006; Blake-Hodek et al., 2010; Irminger-Finger and Mathis, 1998). For example, Bim1 is a microtubule plus end tracking protein (+TIP), present on astral and spindle microtubules where it promotes their assembly through the Bim1-Bik1 complex (Figure S6C) (Blake-Hodek et al., 2010). We identified two dynamic phosphosites in Bim1, S165 known to mediate binding to microtubule, and T249 a novel site located near the EB1-like domain required for interactions with Aurora protein kinase Ipl1, Stu2, Bik1 and itself. Phosphorylation of the S165 residue during anaphase by Aurora kinase unloads Bim1 from microtubules and induces microtubule depolymerization (Zimniak et al., 2009). We could speculate that the dephosphorylation of S165 following osmotic shock could increase the affinity of Bim1 for microtubules and delay their disassembly. This could contribute to preserving the spindle core structure until cells adapt and mitosis can continue following osmotic shock.

## Supplemental References

- Al-Bassam, J., van Breugel, M., Harrison, S.C., and Hyman, A. (2006). Stu2p binds tubulin and undergoes an open-to-closed conformational change. *The Journal of cell biology* *172*, 1009-1022.
- Beltrao, P., Albanese, V., Kenner, L.R., Swaney, D.L., Burlingame, A., Villen, J., Lim, W.A., Fraser, J.S., Frydman, J., and Krogan, N.J. (2012). Systematic functional prioritization of protein posttranslational modifications. *Cell* *150*, 413-425.
- Bennetzen, M.V., Cox, J., Mann, M., and Andersen, J.S. (2012). PhosphoSiteAnalyzer: a bioinformatic platform for deciphering phospho proteomes using kinase predictions retrieved from NetworKIN. *Journal of proteome research* *11*, 3480-3486.
- Blake-Hodek, K.A., Cassimeris, L., and Huffaker, T.C. (2010). Regulation of microtubule dynamics by Bim1 and Bik1, the budding yeast members of the EB1 and CLIP-170 families of plus-end tracking proteins. *Molecular biology of the cell* *21*, 2013-2023.
- Breitkreutz, B.J., Stark, C., and Tyers, M. (2003). The GRID: the General Repository for Interaction Datasets. *Genome biology* *4*, R23.

Chatr-Aryamontri, A., Breitkreutz, B.J., Heinicke, S., Boucher, L., Winter, A., Stark, C., Nixon, J., Ramage, L., Kolas, N., O'Donnell, L., *et al.* (2013). The BioGRID interaction database: 2013 update. *Nucleic acids research* 41, D816-823.

Chou, M.F., and Schwartz, D. (2011). Biological sequence motif discovery using motif-x. Current protocols in bioinformatics / editorial board, Andreas D Baxevanis [et al] *Chapter 13*, Unit 13 15-24.

Chowdhury, S., Smith, K.W., and Gustin, M.C. (1992). Osmotic stress and the yeast cytoskeleton: phenotype-specific suppression of an actin mutation. *The Journal of cell biology* 118, 561-571.

Cline, M.S., Smoot, M., Cerami, E., Kuchinsky, A., Landys, N., Workman, C., Christmas, R., Avila-Campilo, I., Creech, M., Gross, B., *et al.* (2007). Integration of biological networks and gene expression data using Cytoscape. *Nature protocols* 2, 2366-2382.

Cox, J., and Mann, M. (2008). MaxQuant enables high peptide identification rates, individualized p.p.b.-range mass accuracies and proteome-wide protein quantification. *Nature biotechnology* 26, 1367-1372.

Cox, J., Michalski, A., and Mann, M. (2011a). Software lock mass by two-dimensional minimization of peptide mass errors. *Journal of the American Society for Mass Spectrometry* 22, 1373-1380.

Cox, J., Neuhauser, N., Michalski, A., Scheltema, R.A., Olsen, J.V., and Mann, M. (2011b). Andromeda: a peptide search engine integrated into the MaxQuant environment. *Journal of proteome research* 10, 1794-1805.

Franceschini, A., Szklarczyk, D., Frankild, S., Kuhn, M., Simonovic, M., Roth, A., Lin, J., Minguez, P., Bork, P., von Mering, C., *et al.* (2013). STRING v9.1: protein-protein interaction networks, with increased coverage and integration. *Nucleic acids research* 41, D808-815.

Futschik, M.E., and Carlisle, B. (2005). Noise-robust soft clustering of gene expression time-course data. *Journal of bioinformatics and computational biology* 3, 965-988.

Ho, C.H., Magtanong, L., Barker, S.L., Gresham, D., Nishimura, S., Natarajan, P., Koh, J.L., Porter, J., Gray, C.A., Andersen, R.J., *et al.* (2009). A molecular barcoded yeast ORF library enables mode-of-action analysis of bioactive compounds. *Nature biotechnology* 27, 369-377.

Huang da, W., Sherman, B.T., and Lempicki, R.A. (2009a). Bioinformatics enrichment tools: paths toward the comprehensive functional analysis of large gene lists. *Nucleic acids research* 37, 1-13.

Huang da, W., Sherman, B.T., and Lempicki, R.A. (2009b). Systematic and integrative analysis of large gene lists using DAVID bioinformatics resources. *Nature protocols* 4, 44-57.

Irminger-Finger, I., and Mathis, N. (1998). Effect of microtubule-associated protein MHP1 on microtubule assembly and cell cycle progression in *Saccharomyces cerevisiae*. *Cell structure and function* 23, 209-219.

Ishihama, Y., Rappaport, J., and Mann, M. (2006). Modular stop and go extraction tips with stacked disks for parallel and multidimensional Peptide fractionation in proteomics. *Journal of proteome research* 5, 988-994.

Kanshin, E., Michnick, S.W., and Thibault, P. (2013). Displacement of N/Q-rich peptides on TiO<sub>2</sub> beads enhances the depth and coverage of yeast phosphoproteome analyses. *Journal of proteome research* 12, 2905-2913.

Kumar, L., and Futschik, M.E. (2007). Mfuzz: a software package for soft clustering of microarray data. *Bioinformation* 2, 5-7.

Landry, C.R., Levy, E.D., and Michnick, S.W. (2009). Weak functional constraints on phosphoproteomes. *Trends in genetics : TIG* 25, 193-197.

Lee, J., Reiter, W., Dohnal, I., Gregori, C., Beese-Sims, S., Kuchler, K., Ammerer, G., and Levin, D.E. (2013). MAPK Hog1 closes the *S. cerevisiae* glycerol channel Fps1 by phosphorylating and displacing its positive regulators. *Genes & development* 27, 2590-2601.

Linding, R., Jensen, L.J., Pasquale, A., Olhovsky, M., Colwill, K., Bork, P., Yaffe, M.B., and Pawson, T. (2008). NetworKIN: a resource for exploring cellular phosphorylation networks. *Nucleic acids research* 36, D695-699.

Malleshaiah, M.K., Shahrezaei, V., Swain, P.S., and Michnick, S.W. (2010). The scaffold protein Ste5 directly controls a switch-like mating decision in yeast. *Nature* 465, 101-105.

McCleland, M.L., Gardner, R.D., Kallio, M.J., Daum, J.R., Gorbsky, G.J., Burke, D.J., and Stukenberg, P.T. (2003). The highly conserved Ndc80 complex is required for kinetochore assembly, chromosome congression, and spindle checkpoint activity. *Genes & development* 17, 101-114.

Moseley, J.B., and Goode, B.L. (2005). Differential activities and regulation of *Saccharomyces cerevisiae* formin proteins Bni1 and Bnr1 by Bud6. *The Journal of biological chemistry* 280, 28023-28033.

Nock, R., and Nielsen, F. (2006). On weighting clustering. *IEEE transactions on pattern analysis and machine intelligence* 28, 1223-1235.

Rappaport, J., Ishihama, Y., and Mann, M. (2003). Stop and go extraction tips for matrix-assisted laser desorption/ionization, nanoelectrospray, and LC/MS sample pretreatment in proteomics. *Analytical chemistry* 75, 663-670.

Reiter, W., Anrather, D., Dohnal, I., Pichler, P., Veis, J., Grotli, M., Posas, F., and Ammerer, G. (2012). Validation of regulated protein phosphorylation events in yeast by quantitative mass spectrometry analysis of purified proteins. *Proteomics* 12, 3030-3043.

Richardson, H., Lew, D.J., Henze, M., Sugimoto, K., and Reed, S.I. (1992). Cyclin-B homologs in *Saccharomyces cerevisiae* function in S phase and in G2. *Genes & development* 6, 2021-2034.

Schwammle, V., and Jensen, O.N. (2010). A simple and fast method to determine the parameters for fuzzy c-means cluster analysis. *Bioinformatics* 26, 2841-2848.

Schwartz, D., and Gygi, S.P. (2005). An iterative statistical approach to the identification of protein phosphorylation motifs from large-scale data sets. *Nature biotechnology* 23, 1391-1398.

Shannon, P., Markiel, A., Ozier, O., Baliga, N.S., Wang, J.T., Ramage, D., Amin, N., Schwikowski, B., and Ideker, T. (2003). Cytoscape: a software environment for integrated models of biomolecular interaction networks. *Genome research* 13, 2498-2504.

Sheff, M.A., and Thorn, K.S. (2004). Optimized cassettes for fluorescent protein tagging in *Saccharomyces cerevisiae*. *Yeast* 21, 661-670.

Smoot, M.E., Ono, K., Ruscheinski, J., Wang, P.L., and Ideker, T. (2011). Cytoscape 2.8: new features for data integration and network visualization. *Bioinformatics* 27, 431-432.

Soufi, B., Kelstrup, C.D., Stoehr, G., Fröhlich, F., Walther, T.C., and Olsen, J.V. (2009). Global analysis of the yeast osmotic stress response by quantitative proteomics. *Molecular BioSystems* 5, 1337-1346.

Tarassov, K., Messier, V., Landry, C.R., Radinovic, S., Serna Molina, M.M., Shames, I., Malitskaya, Y., Vogel, J., Bussey, H., and Michnick, S.W. (2008). An *in vivo* map of the yeast protein interactome. *Science* 320, 1465-1470.

Willbrand, K., Radvanyi, F., Nadal, J.P., Thiery, J.P., and Fink, T.M. (2005). Identifying genes from up-down properties of microarray expression series. *Bioinformatics* 21, 3859-3864.

Ye, J., Coulouris, G., Zaretskaya, I., Cutcutache, I., Rozen, S., and Madden, T.L. (2012). Primer-BLAST: a tool to design target-specific primers for polymerase chain reaction. *BMC bioinformatics* 13, 134.

Zimniak, T., Stengl, K., Mechtler, K., and Westermann, S. (2009). Phosphoregulation of the budding yeast EB1 homologue Bim1p by Aurora/Ipl1p. *The Journal of cell biology* 186, 379-391.